# Analytical solution for converging elliptic shear wave in a bounded transverse isotropic viscoelastic material with nonhomogeneous outer boundary

Martina Guidetti and Thomas J. Royston[a)]
*Richard and Loan Hill Department of Bioengineering, 851 South Morgan Street, MC 063, University of Illinois at Chicago, Chicago, Illinois 60607, USA*

(Received 26 May 2018; revised 25 August 2018; accepted 28 September 2018; published online 22 October 2018)

Dynamic elastography methods—based on optical, ultrasonic, or magnetic resonance imaging—are being developed for quantitatively mapping the shear viscoelastic properties of biological tissues, which are often altered by disease and injury. These diagnostic imaging methods involve analysis of shear wave motion in order to estimate or reconstruct the tissue's shear viscoelastic properties. Most reconstruction methods to date have assumed isotropic tissue properties. However, application to tissues like skeletal muscle and brain white matter with aligned fibrous structure resulting in local transverse isotropic mechanical properties would benefit from analysis that takes into consideration anisotropy. A theoretical approach is developed for the elliptic shear wave pattern observed in transverse isotropic materials subjected to axisymmetric excitation creating radially converging shear waves normal to the fiber axis. This approach, utilizing Mathieu functions, is enabled via a transformation to an elliptic coordinate system with isotropic properties and a ratio of minor and major axes matching the ratio of shear wavelengths perpendicular and parallel to the plane of isotropy in the transverse isotropic material. The approach is validated via numerical finite element analysis case studies. This strategy of coordinate transformation to equivalent isotropic systems could aid in analysis of other anisotropic tissue structures. 
https://doi.org/10.1121/1.5064372

[GH] Pages: 2312–2323

## I. INTRODUCTION

### A. Background and motivation

Dynamic elastography methods—based on optical, ultrasonic, and magnetic resonance imaging modalities—are being developed for quantitatively mapping the shear viscoelastic properties of biological tissue, which are often altered by disease and injury. Optical methods span from early work using stroboscopy[1] to more recent, higher resolution methods using optical coherence tomography[2,3] or laser Doppler vibrometry[4] to quantitatively map tissue viscoelastic properties at or near the surface, such as the skin or cornea. Ultrasound (US)-based elastography has been implemented a number of different ways using continuous or transient excitation.[5–9] Magnetic resonance elastography (MRE) was introduced in 1995.[10] Optical methods have the advantage of high resolution but little penetration depth; US methods provide high resolution for peripheral regions with limits on penetration depth. MRE has the advantage of greater depth of penetration, even behind hard tissue obstacles such as the skull, and the ability to encode oscillatory motion in all three dimensions simultaneously;[11] however, MRE is limited in resolution as compared to optical methods and is a more expensive measurement to acquire compared to other modalities.

Regardless of imaging modality, dynamic elastography methods share some common traits. They typically involve mechanical stimulation followed by measurement and analysis of resulting shear wave motion in order to estimate or reconstruct the tissue's shear viscoelastic properties. Most initial studies have focused on larger organs, such as the liver or brain, and often made an assumption of isotropic tissue properties in their analysis.

However, application of dynamic elastography to tissues with aligned fibrous structure resulting in local transverse isotropic mechanical properties, such as can be found in striated skeletal and cardiac muscle as well as brain white matter, may benefit from analysis that takes into consideration anisotropy of the tissue. Recognizing this, many groups have pioneered research in this direction over the past few decades, using US-based elastography,[9,12–19] as well as magnetic resonance (MR) based elastography.[20–32] Many of these studies have tried to tackle the associated inversion problem. Multiple configurations or a multi-directional shear wave excitation source may be needed in order to generate and measure shear wave motion that will be affected by its displacement polarization direction and propagation direction in an anisotropic material.

Inversion algorithms employed in most elastography research studies have neglected finite boundary effects. Suppression of boundary effects is attempted via directional filtering of the propagating shear waves and removal of compression waves by taking the curl of the displacement measurements, which requires estimating multiple spatial derivatives of the displacement field. Estimates in the near vicinity of boundaries are also known to be erroneous and it

a)Electronic mail: troyston@uic.edu

is common practice to "erode" layers of pixels near boundaries or tissue interfaces.[33–35] These image processing strategies introduce approximations into the analysis and have limited capability, particularly when boundary effects are significant, creating multiple reflections and mode conversion.

Numerical finite element (FE) techniques have been useful in evaluating and comparing inversion algorithms, and in some cases have themselves been integrated into iterative inversion algorithms.[4,19,36–38] Typically, the FE simulation provides a forward model to calculate displacements based on assumed material parameters. These are then compared to the measured displacements, and the material parameters are iteratively updated based on differences between simulation and experiment until suitable convergence is reached. Other analytical and numerical simulation strategies that are more computationally efficient than FE algorithms have been developed for calculating direction-dependent shear wave group and phase velocities and simulating shear wave propagation (in the absence of significant boundary effects), including in transversely isotropic elastic or viscoelastic materials.[9,39,40]

Theoretical (analytical) solutions, when available, can potentially provide greater insight, solution speed, and ease in conducting parametric or iterative optimization studies, as compared to more computationally-intensive numerical methods. Theoretical solutions for the forward problem, even for simplified ideal geometry, can be invaluable in evaluating inversion methods that can then be applied to experimental data on systems with non-ideal geometry. Theoretical solutions for the shear wave field have been developed for simple geometries with simplifying assumptions, such as neglecting boundaries all together[41] or assuming a semi-infinite half-space.[42] More recently, exact theoretical solutions have been developed and validated for specific experimental configurations for elastography measurements of isotropic materials in a test tube or other cylindrically-shaped container.[43–46] These are useful in assessing the quality of numerical inversion algorithms that can then be applied to more complex geometries, including *in vivo*, where the theoretical solution is not possible.

Continuous oscillatory motion of the test tube or cylindrical specimen holder along its axis sets up a standing shear wave pattern within the test material. Radial convergence of the shear wavefront counterbalances attenuation caused by viscous losses in the material. Measurable shear wave motion can thus be established throughout the entire specimen. Validation of a theoretical solution for an isotropic homogeneous viscoelastic material[43] has been followed by validation of theoretical solutions for nonhomogeneous, but still axisymmetric, composite test materials comprised of concentric annular regions[44] or a spherical region[45] of differing material properties.

To the best of the authors' knowledge, such a closed form theoretical solution has not been presented and validated for the case of a transversely isotropic material. Thus, a simple analytical means of validating newly-developed inversion algorithms for anisotropic materials taking into consideration boundary effects is lacking. Specifically, consider that the material is oriented within the cylindrically-shaped container with its fiber axis normal to the container axis. Shear waves with motion normal to the fiber axis will be generated, but will propagate at different angles relative to the fibers, ranging from parallel to perpendicular. Consequently, propagation speeds and wavelengths will vary circumferentially, resulting in a nonaxisymmetric standing shear wave pattern that can become quite complex and not at all cylindrical.

### B. Objectives

A theoretical approach is proposed for the shear wave pattern observed in transversely isotropic materials subjected to axisymmetric excitation normal (perpendicular) to the axis of isotropy. Radially converging waves driven by axial oscillation of a rigid cylindrical boundary are considered (Fig. 1). The theoretical solution is validated via numerical finite element analysis (FEA) studies.

## II. THEORY

### A. Equations for nearly incompressible transverse isotropic linear viscoelastic material

Building upon Tweten *et al.*,[29,30] we start with a *linear elastic incompressible, transversely isotropic (ITI)* material as our model for biological tissue with aligned fibrous structure subjected to deformation that is sufficiently small in amplitude to justify the assumption of linearity. A linear elastic ITI material may be fully described using three parameters which can be a combination of two tensile moduli, $E_\perp$ *and* $E_\parallel$, and two shear moduli, $\mu_\perp$ *and* $\mu_\parallel$, where the subscripts denote whether the principle direction is perpendicular or parallel to the fiber direction. In other words, $E_\perp$ *and* $\mu_\perp$ are in the direction perpendicular to the fibers (parallel to the plane of isotropy), and $E_\parallel$ *and* $\mu_\parallel$ are in the direction parallel to the fibers (parallel to the axis of isotropy). We define shear anisotropy $\phi = \mu_\parallel/\mu_\perp - 1$ and tensile anisotropy $\zeta = E_\parallel/E_\perp - 1$. Note also that[28] $E_\parallel = \mu_\perp(4\zeta + 3)$; thus, there are only three independent parameters.

Consider a shear wave traveling in an ITI material with an arbitrary propagation direction that is an angle $\theta$ from the fiber direction. The displacement of this shear wave can be polarized into independent slow and fast shear wave components. The polarization direction of the slow shear wave occurs in the direction perpendicular to both the fiber direction and the propagation direction. If the fibers are in the $y$ direction and propagation is in the $x$–$y$ plane, the polarization will be in the $z$ direction for the slow shear wave. Because the slow shear wave does not stretch the fibers, the speed of the slow shear wave $c_s$ only depends on the shear anisotropy and is given by

$$c_s^2 = \frac{\mu_\perp}{\rho}\left(1 + \phi\cos^2[\theta]\right). \tag{1}$$

The corresponding slow shear wavelength $\lambda_s$ at frequency $f$ in Hertz is given by $\lambda_s = c_s/f$ and the corresponding wavenumber is $k_s = 2\pi/\lambda_s$. The ratio of the slow shear

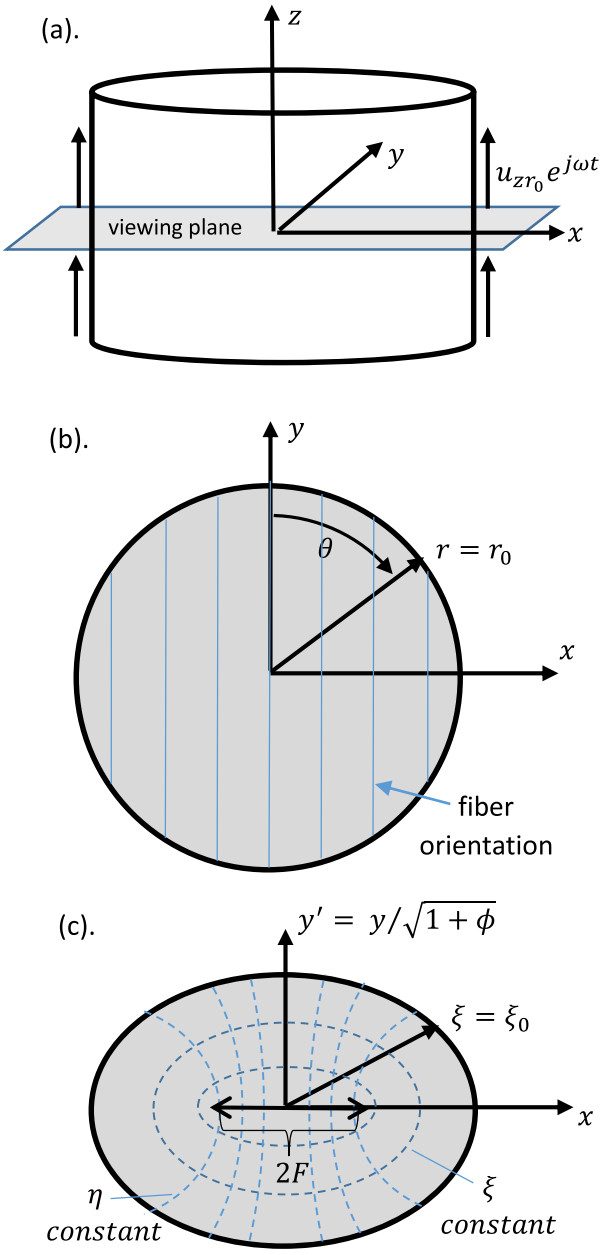


FIG. 1. (Color online) Transversely isotropic cylindrical sample with $x$–$z$ plane of isotropy (fibers in the $y$ direction) subjected to a nonhomogeneous boundary condition: harmonic displacement in the $z$ direction of amplitude $u_{zr_0}$ at frequency $f = \omega/2\pi$ on its curved boundary at $r = r_0$: (a) a three-dimensional rendering with the $x, y$ "viewing plane" indicated, which is the plane used for Figs. 2 and 5; (b) viewed in $x, y$ plane, which is a plane of symmetry; fibers shown along the $y$ axis, the axis of isotropy; (c) viewed in $x, y'$ plane after transformation to an elliptic coordinate system $\{\xi, \eta\}$ with isotropic material properties.

wavelength parallel to the fibers $\lambda_{s\|}$ to the slow shear wavelength perpendicular to the fibers $\lambda_{s\perp}$ is $\lambda_{s\|}/\lambda_{s\perp} = \sqrt{1+\phi}$.

On the other hand, for the case of the fast shear wave whose polarization direction is perpendicular to the propagation direction but also perpendicular to the slow shear wave polarization direction, and thus not perpendicular to the fiber direction, we have the speed of the fast shear wave $c_f$ given by

$$c_f^2 = \frac{\mu_\perp}{\rho}\left(1 + \phi\cos^2[2\theta] + \zeta\sin^2[2\theta]\right). \tag{2}$$

The corresponding fast shear wavelength $\lambda_f$ at frequency $f$ in Hertz is given by $\lambda_f = c_f/f$. Note that if $\zeta = \phi$ then $c_f = \sqrt{\mu_\perp/\rho(1+\phi)}$ or, in other words, $\lambda_f = \lambda_{s\|}$ regardless of $\theta$. If $\zeta \neq \phi$ the relationship is more complex. Please see the Appendix for additional background.

With respect to propagation of shear waves over a broad frequency range, soft biological tissue is not linear elastic, but rather linear *viscoelastic*, experiencing rate-dependent energy loss (dissipated as heat) as the wave propagates through the material. Linear viscoelasticity can be accounted for in the above formulation by defining $\mu_\perp = \mu_{\perp R} + j\mu_{\perp I}$ and $\mu_\| = \mu_{\|R} + j\mu_{\|I}$, where $j = \sqrt{-1}$ and the real parts of $\mu_\perp$ *and* $\mu_\|$ denote the shear storage moduli and the imaginary parts denote the shear loss moduli. Both shear storage and loss moduli may be a function of frequency $f$, possibly governed by a rheological model that establishes their dependence on frequency. With the introduction of complex values for the shear modulus, the corresponding expression for the slow shear wavelengths perpendicular and parallel to the fibers become[47]

$$\lambda_\perp = \frac{1}{f}\sqrt{\frac{2}{\rho}\frac{\mu_{\perp R}^2 + \mu_{\perp I}^2}{\mu_{\perp R} + \sqrt{\mu_{\perp R}^2 + \mu_{\perp I}^2}}}, \tag{3}$$

$$\lambda_\| = \frac{1}{f}\sqrt{\frac{2}{\rho}\frac{\mu_{\|R}^2 + \mu_{\|I}^2}{\mu_{\|R} + \sqrt{\mu_{\|R}^2 + \mu_{\|I}^2}}}. \tag{4}$$

### B. Converging shear waves in a finite cylindrical region

One means of creating steady state harmonic shear wave motion is to apply motion of amplitude $u_{zr_0}$ in the $z$ direction over a cylindrical surface of radius $r_0$ with axis aligned with the z axis, as illustrated in Fig. 1,

$$u_z[r = r_0, t] = Real\left[u_{zr_0}e^{j\omega t}\right]. \tag{5}$$

Here and henceforth, the fact that the *real* part is of interest will be implicit.

This type of vibratory excitation has been used in previous studies to create a shear wave field within an excised biological specimen or tissue phantom material placed within a cylindrical test tube.[11,43–46,48–50] The tube itself is harmonically driven along its axis. The inner wall of the test tube serves as the nonhomogeneous displacement boundary condition applied to the material within it.

For an *isotropic* and homogeneous material in the test tube, the following theoretical solution governs steady state shear wave motion at any location within the test tube, $r < r_0$:

$$u_z[r, t] = u_{zr_0}\frac{J_0[k_s r]}{J_0[k_s r_0]}e^{j\omega t}. \tag{6}$$

Here, $J_0$ is the zeroth order Bessel function of the first kind. This solution follows from the condition of axisymmetry established by the isotropic, homogeneous medium confined

within a cylindrical geometry with an axisymmetric boundary condition that eliminates higher order Bessel functions that will have $\theta$ dependence, and the need for a finite solution at the origin that eliminates Bessel functions of the second kind.

In the case of *transverse isotropy* with the $y$ axis as the axis of isotropy, axisymmetry is destroyed and Eq. (6) is no longer valid. Now consider a transformation to a new Cartesian coordinate system, with $y$ replaced by $y' = y/\sqrt{1+\phi}$ for a purely elastic case or for the case that the ratio of shear loss to storage moduli are the same in parallel and perpendicular directions: $\eta = \mu_{\perp I}/\mu_{\perp R} = \mu_{\parallel I}/\mu_{\parallel R}$. If these ratios are not the same, for the more general viscoelastic case we will divide $y$ by the ratio of shear wavelength along the fiber direction with respect to the shear wavelength perpendicular to the fiber direction, where shear wavelength perpendicular and parallel to the fiber direction are given by Eqs. (3) and (4), respectively. Thus, for the general viscoelastic case we have

$$y' = y\sqrt{\left(\frac{\mu_{\perp R}^2+\mu_{\perp I}^2}{\mu_{\parallel R}^2+\mu_{\parallel I}^2}\right)\left(\frac{\mu_{\parallel R}+\sqrt{\mu_{\parallel R}^2+\mu_{\parallel I}^2}}{\mu_{\perp R}+\sqrt{\mu_{\perp R}^2+\mu_{\perp I}^2}}\right)}. \tag{7}$$

Note, as shear wave speed is simply shear wavelength multiplied by the frequency of oscillation in Hertz, one gets the same ratio if one were to use shear wave speed along the fiber direction with respect to perpendicular to the fiber direction, in place of wavelengths. In this new coordinate system, shear waves propagating in the $\{x, y'\}$ plane polarized in the $z$ direction will all propagate at the same phase speed, with the same wavelength at a given frequency, independent of the direction of propagation $\theta$. In the transformed coordinate system, this shear wave behavior is isotropic. However, the same length distortion must be applied to the cylindrical boundary condition at $r = r_0$, which is now an elliptic boundary condition at $\xi = \xi_0$ in the $\{x, y'\}$ coordinate system. Specifically, in order to create isotropy, for the case of elasticity or constant $\eta$, we are distorting space as a function of $\theta$ by reducing length by a factor of $\sqrt{1+\phi\cos[\theta]^2}$ where $\theta$ denotes the direction with respect to the fiber axis. This is exactly an elliptic coordinate system.

Thus, this can be transformed to elliptic coordinates $\{\xi, \eta\}$ such that $x = F\cosh[\xi]\cos[\eta]$, and $y' = F\sinh[\xi]\sin[\eta]$ where $F = r_0/\cosh[\xi_0] = r_0/\sqrt{\phi}/\sinh[\xi_0]$, $0 \le \eta \le 2\pi$, $0 \le \xi \le \xi_0$. The coordinates $\{\xi, \eta\}$ and the distance from the origin to each focal point, F, are indicated in Fig. 1(c). The nonhomogeneous boundary condition replacing Eq. (5) is

$$u_z[\xi = \xi_0, t] = u_{zr_0}e^{j\omega t}. \tag{8}$$

Shear wave motion propagating in the $\{x, y'\}$ plane with $z$ polarization can be expressed in terms of angular and radial Mathieu functions[51,52] via a separation of variables approach to the governing partial differential equation, in a way analogous to how sinusoidal and Bessel functions are used to construct shear wave motion subject to a cylindrical boundary condition.[53] The imposed displacement on the elliptic boundary allows only for Mathieu functions that have even parity with periodicity of $\pi$ radians. Unlike in the case of cylindrical coordinates, there is no single member of the Mathieu function set that can satisfy the imposed boundary condition. Rather, an infinite summation of functions is needed such that

$$\frac{u_z[\xi,\eta]}{u_z[\xi_0,\eta]} = 2\sum_{n=0}^{\infty} A_0^{2n}[q]\frac{Je_{2n}[\xi,q]}{Je_{2n}[\xi_0,q]}ce_{2n}[\eta,q], \tag{9}$$

where we have from Eq. 28.11.3 of Ref. 54,

$$1 = 2\sum_{n=0}^{\infty} A_0^{2n}[q]ce_{2n}[\eta,q]. \tag{10}$$

Here, $Je_{2n}[\xi,q]$ and $ce_{2n}[\eta,q]$ are the even parity radial (modified) and angular Mathieu functions of the first kind, respectively, of periodicity $\pi$ radians. And, $\xi_0 = arc\tan h[1/\sqrt{\phi}]$, $q = (Fk/2)^2$, and $k = \omega\sqrt{\rho/\mu_\perp}$. Here, $q$ is known as a Mathieu parameter and its value and that of $F$ increase with the degree of shear anisotropy $\phi$. For the isotropic case, both are zero and the angular and radial Mathieu functions collapse to sinusoidal and Bessel functions, respectively, exactly matching isotropic theory. Coefficients $A_0^{2n}[q]$ for $n = 0, 1, 2,\ldots$ can be approximated by solving the following eigenvalue problem, which will have $n = 1,\ldots,N$ solutions for the eigenvalue $a$ with $n = 1,\ldots,N$ corresponding eigenvectors of length $N$:[55]

$$\begin{bmatrix} -a & q & 0 & 0 & 0 & 0 & \cdots \\ 2q & 2^2-a & q & 0 & 0 & 0 & \cdots \\ 0 & q & 4^2-a & q & 0 & 0 & \cdots \\ 0 & 0 & q & 6^2-a & q & 0 & \cdots \\ \vdots & \vdots & \vdots & \vdots & \vdots & \vdots & \ddots \end{bmatrix}\begin{bmatrix} A_0^{2n} \\ A_2^{2n} \\ A_4^{2n} \\ A_6^{2n} \\ \vdots \end{bmatrix} = 0. \tag{11}$$

Note, while Eq. (11) asymptotically yields the exact solution for positive real-valued $q$, for the case of complex-valued $q$ with a positive real part, as is ours since $\mu$ is complex-valued, there is some error in the approximation; the impact of this is reviewed in the results and discussion sections below.

While the summations in Eqs. (9) and (10) are infinite, as $n$ increases, the magnitude of $A_0^{2n}[q]$ significantly decreases such that the summation can be truncated. In the results presented in Sec. III, $N = 10$ eigenvectors were calculated and the presented results are based on summing Eq. (9) to this value. It was confirmed that increasing $N$ further had a negligible effect.

## III. NUMERICAL VALIDATION CASE STUDIES

The theoretical approach described in Sec. II was implemented for specific case studies in MATLAB Version 16.a (Mathworks Inc., Natick, MA) utilizing a free downloadable Mathieu function toolbox.[55] To validate the theoretical

TABLE I. Geometrical and material parameter values for case studies.

| Parameter | Nomenclature | Value(s) |
|---|---|---|
| Cylinder radius | $r_0$ | 4 mm |
| Shear storage modulus in plane of isotropy | $\mu_{\perp R}$ | 2.77 kPa |
| Ratio of shear loss to storage moduli | $\eta = \mu_{\perp I}/\mu_{\perp R} = \mu_{\parallel I}/\mu_{\parallel R}$ | 0.01 or 0.15 |
| Shear anisotropy | $\phi$ | 0.1 or 1 |
| Density | $\rho$ | 1000 kg/m$^3$ |
| Frequency | $f$ | 1 kHz |

approach, predictions from it were compared to those from computational FEA.

The case study configuration is based on an experimental setup used by our group and others to conduct MRE on biological tissue and phantom material specimens, utilizing geometrically focused (radially converging) shear wave excitation.[11,43–46,48–50] Geometry and material property values, which are typical of soft biological tissue and tissue phantoms (for the case $\eta = 0.15$) are provided in Table I. The theoretical solution assumes the cylinder has infinite height along its principle axis in the $z$ direction. However, in the FE model, it is 20 mm in height, with the upper and lower surfaces having free boundary conditions. These finite boundary conditions coupled with the nonhomogeneous boundary condition of vertical oscillatory motion $u_{zr_0}e^{j\omega t}$ on the outer curved boundary of the cylinder result in standing Rayleigh-Lamb (RL) waves.[50,56] However, with the given dimensions and wavelengths, the differences between these RL waves and shear waves in the infinite height cylinder are expected to be small, though non-negligible, except in the vicinity of RL wave resonant frequencies under lightly damped cases.

A numerical FE study using harmonic analysis (steady state response equivalent to a particular solution in the frequency domain) was conducted using COMSOL Mulitphysics Version 5.3 (COMSOL, Burlington, MA) software. The automatically meshed model contained 46 724 vertices, 267 162 quadratic tetrahedral elements (0.004 to 0.4 mm in size), 9152 triangular elements, 328 edge elements, and 8 vertex elements. The minimum and average element quality were 0.176 and 0.662, respectively. The element volume ratio was 0.0565 and the mesh volume was 1004 mm$^3$. (Mesh resolution was decided upon when further increases had a negligible effect on the solution.) Typical computation times for the single frequency harmonic analysis were about 30 min using a 64-bit operating system, x64 based processor, Intel® Xeon® CPU E5-2609 0 with a clock speed of 2.40 GHz, and 256 GB RAM. The theoretical

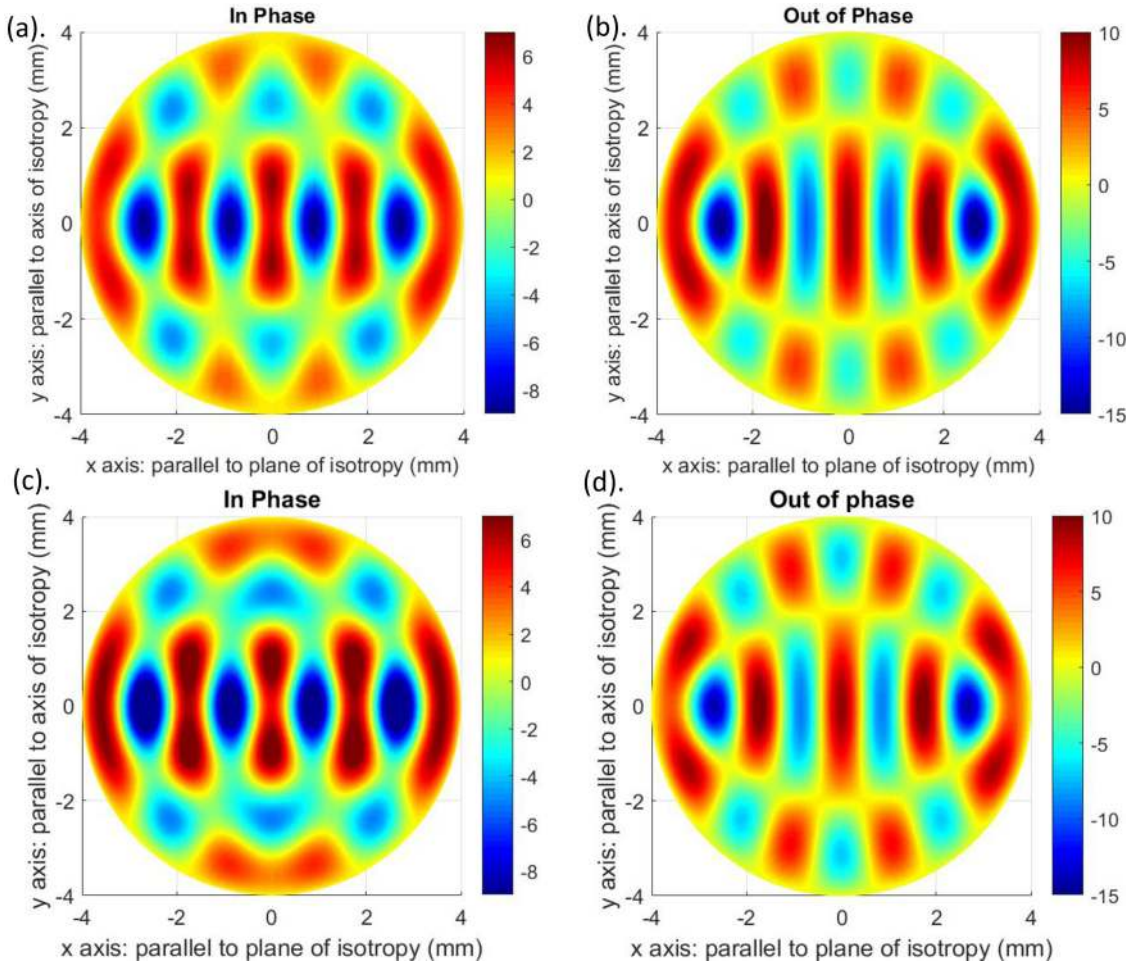


FIG. 2. (Color online) Normalized $z$ direction displacement $(u_{zr}/u_{zr_0})$ on the $x$–$y$ plane for the case $\phi = 1$ and $\eta = 0.01$ using the theoretical model [(a) in phase, (b) 90 degrees out of phase] and the FE model [(c) in phase, (d) 90 degrees out of phase]. See supplementary material (Ref. 57).

approach used to calculate the results presented below took about a second in MATLAB.

According to Sec. II, for the given configuration that only excites slow shear waves, the value of $\zeta$ is not relevant. FE simulations using different values of $\zeta$ from 0 to 2 confirmed this. Also, while the theory described in Sec. II assumes incompressibility, the FE simulations did not make this assumption. Rather, the material was modeled using the bulk modulus of water $\kappa = 2.15\,\text{GPa}$. As the bulk modulus is nearly six orders of magnitude greater than the shear moduli, the Poisson's ratio $\nu$ will be nearly equal to but less than 0.5. The orthotropic elasticity matrix $\boldsymbol{K}$ using Voigt notation and nomenclature from Schmidt *et al.*,[28] but taking the fiber orientation to be parallel to the $y$ axis, in COMSOL is

$$\boldsymbol{K} = \begin{bmatrix} \kappa + \mu_\perp\left(\frac{4}{3}+\frac{4}{9}\zeta\right) & \kappa - \mu_\perp\left(\frac{2}{3}+\frac{8}{9}\zeta\right) & \kappa - \mu_\perp\left(\frac{2}{3}-\frac{4}{9}\zeta\right) & 0 & 0 & 0 \\ \kappa - \mu_\perp\left(\frac{2}{3}+\frac{8}{9}\zeta\right) & \kappa + \mu_\perp\left(\frac{4}{3}+\frac{16}{9}\zeta\right) & \kappa - \mu_\perp\left(\frac{2}{3}+\frac{8}{9}\zeta\right) & 0 & 0 & 0 \\ \kappa - \mu_\perp\left(\frac{2}{3}-\frac{4}{9}\zeta\right) & \kappa - \mu_\perp\left(\frac{2}{3}+\frac{8}{9}\zeta\right) & \kappa + \mu_\perp\left(\frac{4}{3}+\frac{4}{9}\zeta\right) & 0 & 0 & 0 \\ 0 & 0 & 0 & \mu_\perp(1+\phi) & 0 & 0 \\ 0 & 0 & 0 & 0 & \mu_\perp & 0 \\ 0 & 0 & 0 & 0 & 0 & \mu_\perp(1+\phi) \end{bmatrix}. \tag{12}$$

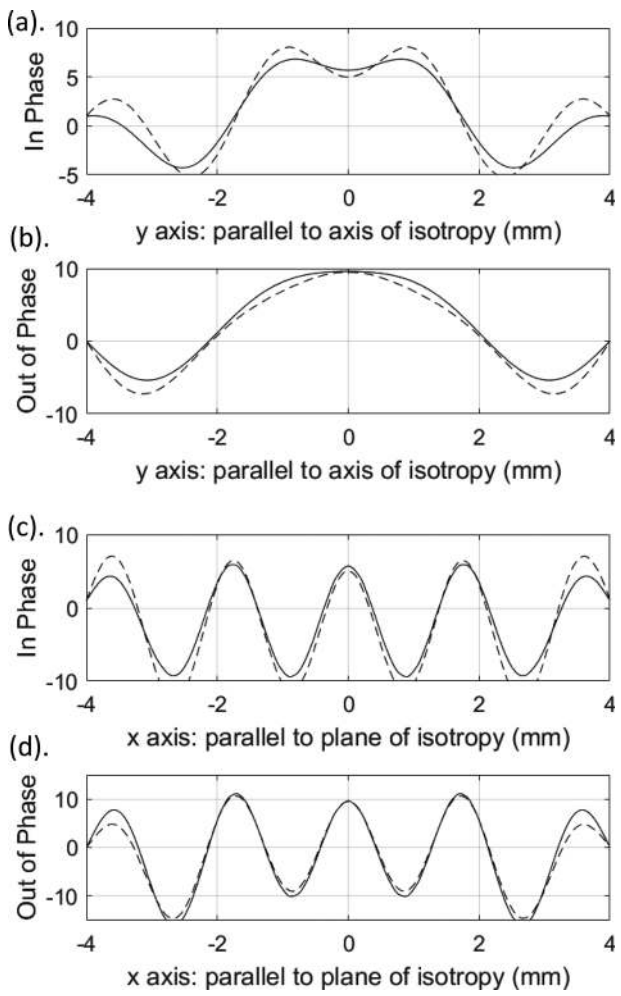


FIG. 3. Normalized $z$ direction displacement $(u_{zr}/u_{zr_0})$ for the case $\phi = 1.0$ and $\eta = 0.01$ using the theoretical model (solid line) and the FE model (dashed line): (a) along the $y$ (fiber) axis in phase: $\Delta_y = 26\%$; (b) along the $y$ (fiber) axis 90 degrees out of phase: $\Delta_y = 16\%$; (c) along the $x$ axis in phase: $\Delta_x = 28\%$ (d) along the $x$ axis 90 degrees out of phase: $\Delta_x = 12\%$.

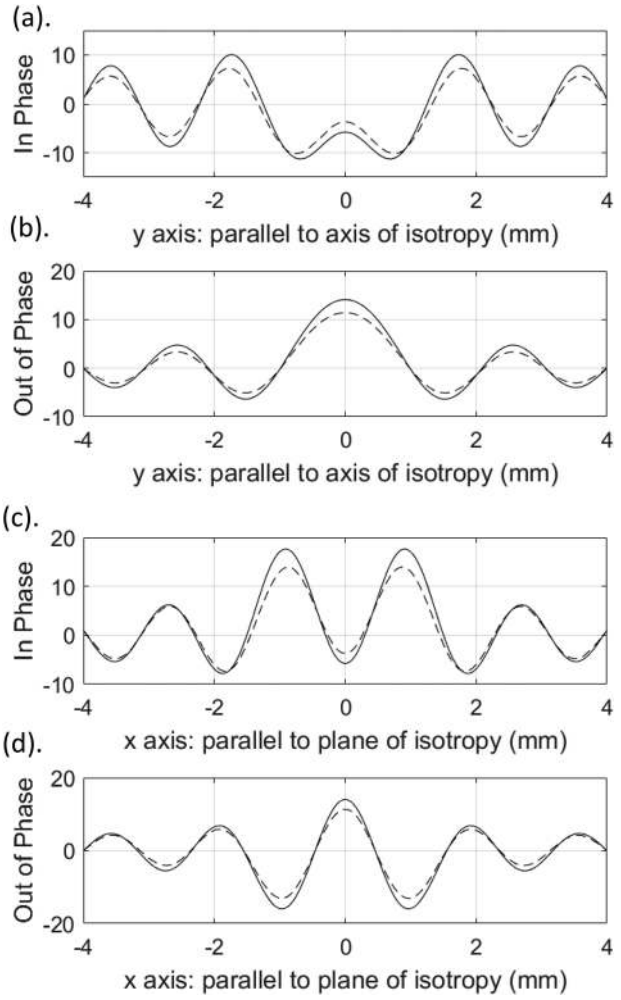


FIG. 4. Normalized $z$ direction displacement $(u_{zr}/u_{zr_0})$ for the case $\phi = 0.1$ and $\eta = 0.01$ using the theoretical model (solid line) and the FE model (dashed line): (a) along the $y$ (fiber) axis in phase: $\Delta_y = 22\%$; (b) along the $y$ (fiber) axis 90 degrees out of phase: $\Delta_y = 17\%$; (c) along the $x$ axis in phase: $\Delta_x = 16\%$; (d) along the $x$ axis 90 degrees out of phase: $\Delta_y = 15\%$.

In Fig. 2, we see a comparison of the theoretical and FE solutions for the normalized $z$ displacement of Eq. (9) on an axial slice ($x$–$y$ plane) in phase and (90 degrees) out of phase with the displacement excitation for the material parameter values in Table I for the case $\eta = 0.01$ and $\phi = 1$. For the FE model, the slice location is at the mid-height level (10 mm). The complex standing wave patterns do not look like simple cylindrical or elliptically converging waves due to interference and multiple reflections at the finite boundaries.

In Figs. 3 and 4, line profiles of the theoretical and FE solutions within the slice in Fig. 2 and along the $x$ and $y$ axes are plotted for $\eta = 0.01$ and the cases of $\phi = 1$ and 0.1, respectively, providing a more direct visual comparison of the theoretical and numerical FE results. The case of $\phi = 0.1$ is included to show that even a small amount of anisotropy can significantly affect the response. The percent difference along the $x$ or $y$ axis, $\Delta_x\%$ or $\Delta_y\%$, between theoretical and FE solutions is calculated for plots shown in Figs. 3 and 4 by taking the mean of the absolute values of the differences in the displacement profiles divided by the root mean square of the theoretical displacement profile. That is,

$$\Delta_x\% = \frac{100}{N_{FEA}} \sum_{i=1}^{N_{FEA}} \sqrt{\frac{\left(u_{zTheory}[x_i, y=0] - u_{zFEA}[x_i, y=0]\right)^2}{\frac{1}{N_{FEA}} \sum_{i=1}^{N_{FEA}} \left(u_{zTheory}[x_i, y=0]\right)^2}}, \tag{13a}$$

$$\Delta_y\% = \frac{100}{N_{FEA}} \sum_{i=1}^{N_{FEA}} \sqrt{\frac{\left(u_{zTheory}[x=0, y_i] - u_{zFEA}[x=0, y_i]\right)^2}{\frac{1}{N_{FEA}} \sum_{i=1}^{N_{FEA}} \left(u_{zTheory}[x=0, y_i]\right)^2}}, \tag{13b}$$

where $i = 1, \ldots, N_{FEA}$ are 300 equally spaced points along the $x$ or $y$ axis from $-r_0$ *to* $+r_0$ for which the vertical displacement, $u_{zFEA}[x = 0, y_i]$ or $u_{zFEA}[x_i, y = 0]$, is obtained from COMSOL and compared to theoretical solutions, $u_{zTheory}[x = 0, y_i]$ or $u_{zTheory}[x_i, y = 0]$, at those exact same points. Differences are divided by the root-mean-square (rms) of the theoretical solution instead of the theoretical solution at that point so as not to amplify differences at locations where $u_{zTheory}$ is equal or nearly equal to zero. These percent differences are provided in the figure captions.

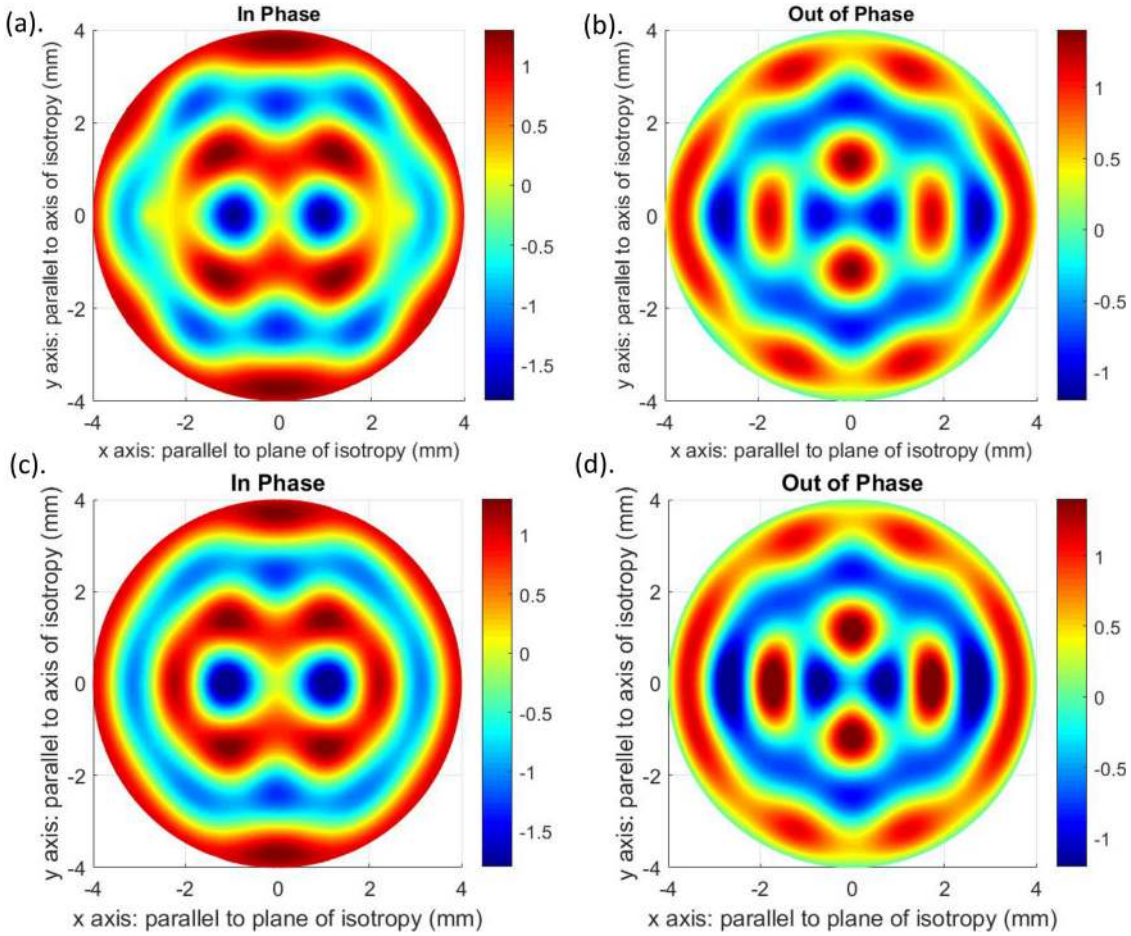


FIG. 5. (Color online) Normalized $z$ direction displacement $(u_{zr}/u_{zr_0})$ on the $x$–$y$ plane for the case $\phi = 1$ and $\eta = 0.15$ using the theoretical model [(a) in phase, (b) 90 degrees out of phase] and the FE model [(c) in phase, (d) 90 degrees out of phase]. See supplementary material (Ref. 57).

In Fig. 5, the same comparison is made as in Fig. 2, except for the case $\phi = 1$ and $\eta = 0.15$, which is a level of viscosity more akin to soft biological tissue. Likewise, in Figs. 6 and 7, the same line profile comparisons are made as in Figs. 3 and 4 except for $\eta = 0.15$ and the cases $\phi = 1$ and 0.1, respectively. While there is general agreement in standing wave pattern shapes between theory and numerical FEA, differences exist that are quantified on a percentage basis for each comparison and provided in the figure captions.

## IV. DISCUSSION

In all cases, there is expected to be some small level of error in the numerical FE simulation; it is an approximation. Additionally, neglecting the effect of finite boundaries on the top and bottom of the cylindrical finite element phantom introduces error into the theoretical solution. Both of these sources of error are thought to be independent of anisotropy but could depend on level of damping (viscosity). Finite boundaries, which produce reflections and mode conversion, will generally have a more pronounced effect when damping

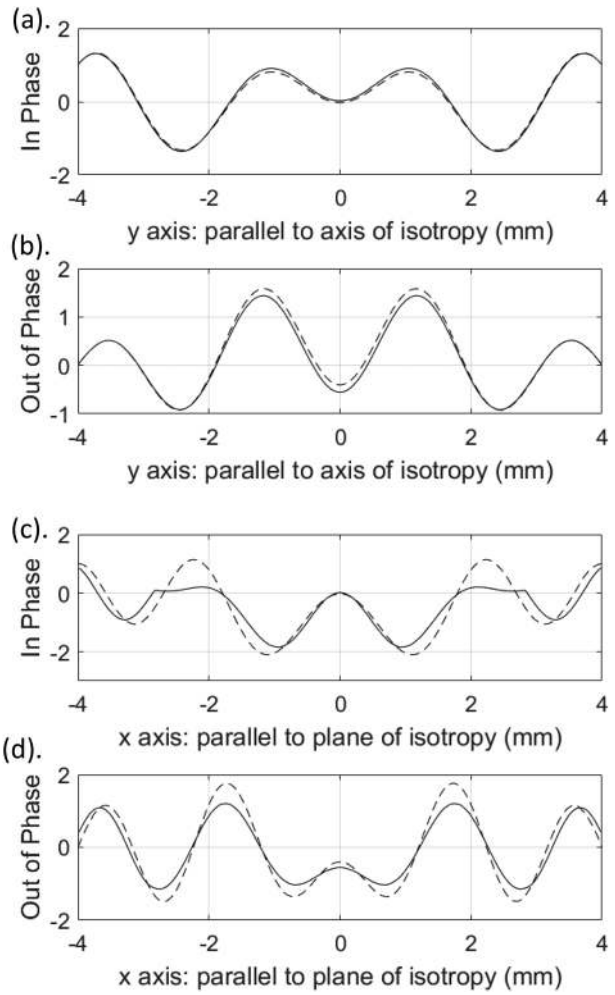


FIG. 6. Normalized $z$ direction displacement $(u_{zr}/u_{zr_0})$ for the case $\phi = 1.0$ and $\eta = 0.15$ using the theoretical model (solid line) and the FE model (dashed line): (a) along the $y$ (fiber) axis in phase: $\Delta_y = 6.0\%$; (b) along the $y$ (fiber) axis 90 degrees out of phase: $\Delta_y = 9.6\%$; (c) along the $x$ axis in phase: $\Delta_x = 41\%$; (d) along the $x$ axis 90 degrees out of phase: $\Delta_x = 31\%$.

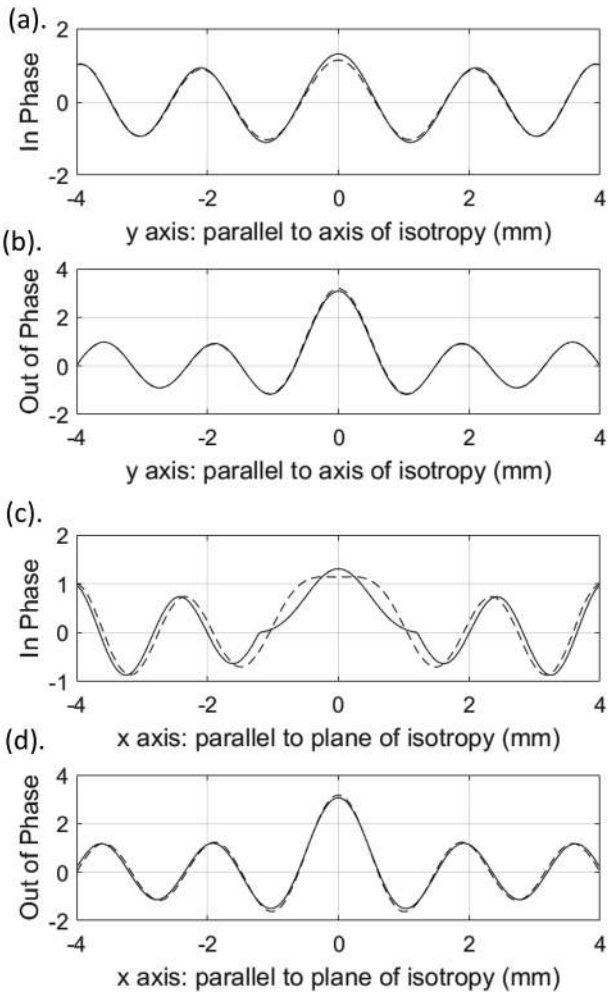


FIG. 7. Normalized $z$ direction displacement $(u_{zr}/u_{zr_0})$ for the case $\phi = 0.1$ and $\eta = 0.15$ using the theoretical model (solid line) and the FE model (dashed line): (a) along the $y$ (fiber) axis in phase: $\Delta_y = 6.3\%$; (b) along the $y$ (fiber) axis 90 degrees out of phase: $\Delta_y = 2.5\%$; (c) along the $x$ axis in phase: $\Delta_x = 29\%$; (d) along the $x$ axis 90 degrees out of phase: $\Delta_x = 7.4\%$.

is less, as wave energy travels further and thus has more opportunities for interaction with boundaries. To quantify the combined effect of error in both the FE and theoretical approaches independent of anisotropy, the case studies of Sec. III with $\eta = 0.01$ and 0.15, but with $\phi = 0$ (isotropic case) were conducted. Plots similar to those shown in Figs. 3 or 4 and 6 or 7 are provided in Figs. 8 and 9. Percent differences between the FE and theoretical solutions were calculated exactly the same way, with the theoretical solution of Eq. (9) now exactly matching Eq. (6). In the isotropic case, normalized $z$ direction displacement $(u_{zr}/u_{zr_0})$ is identical along both the $x$ and $y$ axes $(\Delta_x = \Delta_y = \Delta_r)$; so, only plots along one axis are shown and percent differences are reported in the figure captions, both in phase and out of phase with the excitation.

Aside from the out of phase comparison for non-physiological (low) damping, these percent differences are small, providing confidence in both the FE model and theoretical approach for the case of physiologically relevant damping.[23,28,31,58–61] It is hypothesized that the percent difference for the low damping isotropic case may be worse

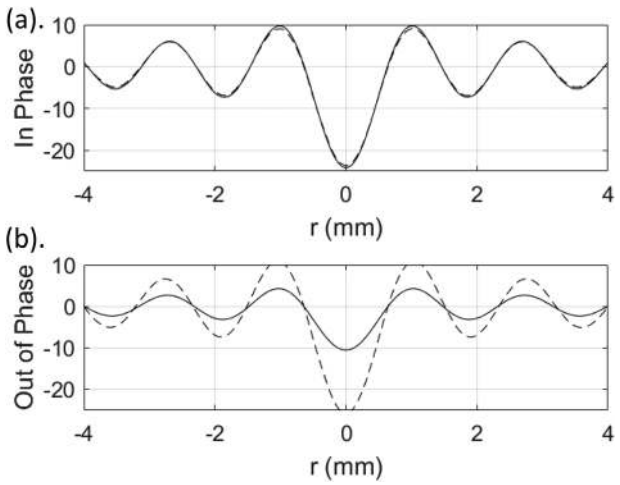


FIG. 8. Normalized $z$ direction displacement $(u_{zr}/u_{zr_0})$ for the case $\phi = 0$ and $\eta = 0.01$ using the theoretical model (solid line) and the FE model (dashed line): (a) along a diameter in phase: $\Delta_r = 3.54\%$; (b) along a diameter 90 degrees out of phase: $\Delta_r = 109\%$.

than in any of the anisotropic cases because axisymmetry amplifies the focusing effect of the radially converging wavefront, which then will interact with the finite boundaries to a greater extent. Moreover, the high out of phase response predicted by FEA for $\eta = 0.01$, which caused the 109% difference, is likely due to resonance near a natural frequency of the finite boundary system, directly dependent on the cylinder's finite height. (Shifting the frequency for the isotropic case to 950 Hz or 1010 Hz reduced this difference to 15% and 8.1%, respectively.) There are Rayleigh-Lamb wave resonances (standing wave patterns) dependent on the cylinder height and not considered in the theoretical solution. Actually, in the isotropic case with axisymmetry, there will be pairs of degenerate modes with repeated natural frequencies. Introducing anisotropy will both split and shift the natural frequencies. In the vicinity of the natural frequency, when damping is low, the response is amplified.[62]

Now referring to the anisotropic cases and the elliptic-based theory, for the case of physiological (significant) damping ($\eta = 0.15$), there is agreement between theory and FE simulation that is better than the non-physiological (low) damping case for small anisotropy ($\phi = 0.01$), but worse than the low damping case when there is increased anisotropy ($\phi = 1$). As noted above, increased damping reduces finite boundary effects (top and bottom of cylinder) and thus brings the FE solution and theory closer together. However, increased damping combined with increased anisotropy amplifies a current limitation of the elliptic-based theoretical solution. As damping and anisotropy increase the imaginary part of the Mathieu parameter, $q$ becomes larger, thus increasing error in the algorithm used to calculate the Mathieu function coefficients $A_0^{2n}[q]$ used in Eqs. (9)–(11). This is the reason for the abrupt discontinuities in slope observed in Figs. 6(c) and 7(c) (which in turn causes $\Delta_x\%$ to exceed $\Delta_y\%$). Additionally, as the imaginary part of $q$ increases the algorithm becomes less able to find a series of coefficient values to exactly satisfy Eq. (10). This resulted in an inability to satisfy the axisymmetric boundary condition on the curved outer surface of the cylinder, which worsened with increasing $\phi$. In Figs. 10 and 11, the calculated displacement at $r = r_0$ is shown both in and out of phase for the cases depicted in Figs. 2 ($\eta = 0.01$) and 5 ($\eta = 0.15$), respectively. In these plots, it is also evident that, unlike the zeroth order Bessel function of the first kind $J_0[k_s r]$ that singlehandedly satisfies the nonhomogeneous axisymmetric boundary condition, for the elliptic case per Eq. (9), it is necessary to have a weighted sum of multiple higher order Mathieu functions.

In documentation provided with the MATLAB functions that were adapted for this study,[55] it is noted that the algorithm is for positive and real values of $q$. However, since $q$ is proportional to the square of the shear wavenumber, which in turn is proportional to the reciprocal of the square root of the shear modulus $\mu$, in the present application, Mathieu

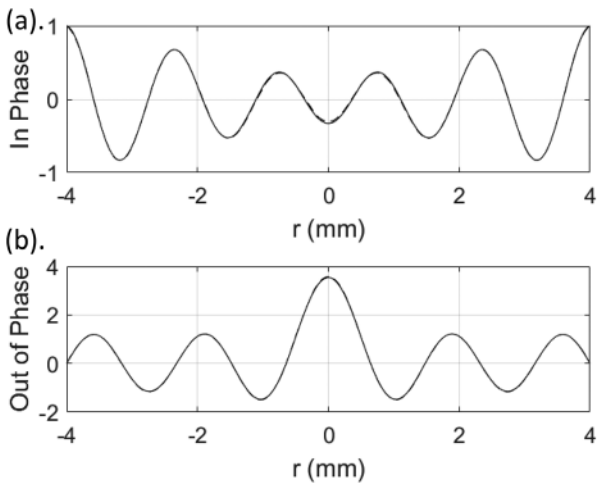


FIG. 9. Normalized $z$ direction displacement $(u_{zr}/u_{zr_0})$ for the case $\phi = 0$ and $\eta = 0.15$ using the theoretical model (solid line) and the FE model (dashed line): (a) along a diameter in phase: $\Delta_r = 1.74\%$; (b) along a diameter 90 degrees out of phase: $\Delta_r = 0.8\%$. (Dashed line difficult to see because of close match).

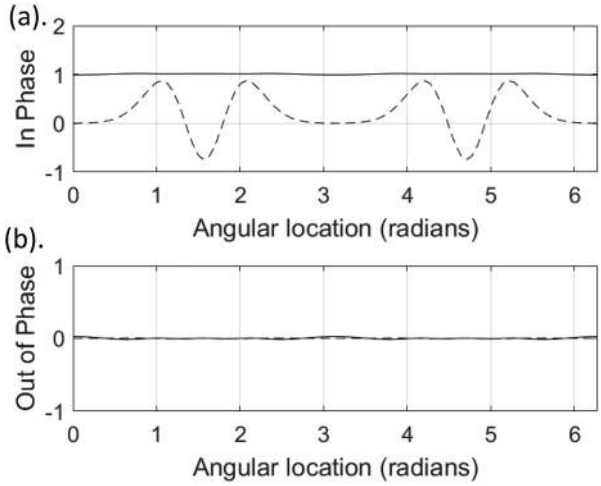


FIG. 10. Normalized $z$ direction displacement $(u_{zr}/u_{zr_0})$ on the outer boundary of the cylinder at $r = r_0$ for $\theta$ from 0 to $2\pi$ radians for the case $\phi = 1$ and $\eta = 0.01$ using the theoretical model [(a) in phase, (b) 90 degrees out of phase]. The solid line is the solution of the summation in Eq. (9) using $n = 0,\ldots, 9$. The dashed line is the first term only ($n = 0$).

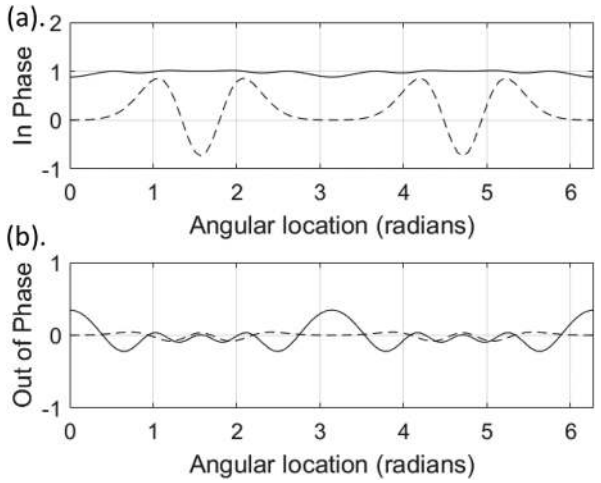


FIG. 11. Normalized $z$ direction displacement $(u_{zr}/u_{zr_0})$ on the outer boundary of the cylinder at $r = r_0$ for $\theta$ from 0 to $2\pi$ radians for the case $\phi = 1$ and $\eta = 0.15$ using the theoretical model [(a) in phase, (b) 90 degrees out of phase]. The solid line is the solution of the summation in Eq. (9) using $n = 0,\ldots, 9$. The dashed line is the first term only ($n = 0$).

parameter $q$ will be complex-valued, since $\mu$ is complex-valued. Mathieu functions are defined and can be determined for complex-valued $q$, at least asymptotically.[54] However, a reliable algorithm for the values needed in the present study has not yet been found or developed by the authors.

Thus, on the one hand, the elastic case will result in real-valued $q$, which one might think would improve the theoretical solution. On the other hand, the purely elastic case in the FE model may allow for Rayleigh-Lamb standing wave patterns (resonant responses) to dominate depending on how close one is to a natural frequency, which is not captured by the proposed theory. Nonetheless, this new theoretical approach, even with the issue of complex-valued $q$, does well for physiologically relevant damping values such as $\eta = 0.15$. Even with the differences noted in particular in Figs. 6(c), 6(d), and 7(c), the overall shape of the standing wave pattern, which is not at all simply circular or elliptic, is captured when comparing Figs. 5(a) and 5(b) to 5(c) and 5(d), respectively. In addition, even in the case of 109% error when $\eta = 0.01$, the standing wave pattern is captured; it is a matter of amplitude difference [Fig. 8(b)].

## V. CONCLUSION

A theoretical solution is developed for the standing shear wave pattern observed in a transverse isotropic material subjected to axisymmetric excitation normal to the fiber axis on a finite cylindrical boundary. The theoretical solution, utilizing Mathieu functions, is enabled via a transformation to an elliptic coordinate system with isotropic properties and a ratio of minor and major axes that matches the ratio of shear wavelengths perpendicular and parallel to the plane of isotropy in the transverse isotropic material. Numerical FEA case studies both validate the theoretical approach and reveal a limitation not of the approach, but rather its implementation in the present article. The algorithm used to calculate Mathieu function values is only strictly valid for real-valued shear wave numbers. This corresponds to the purely elastic (and fictitious) condition. An algorithm valid for complex-valued Mathieu parameter $q$ is needed to generate Mathieu functions for complex-valued shear wavenumbers, which are necessary for viscoelastic modeling. This and exploration of Rayleigh-Lamb wave theory in elliptic coordinates are left for future studies.

The novel strategy introduced in this study of coordinate transformation to convert an anisotropic problem into an isotropic one, albeit with more complex boundary conditions, could be expanded to analysis of other anisotropic tissue structures and experimental configurations and geometries. Also left for future development is the possibility of an inversion algorithm directly based on this coordinate transformation strategy. Nonetheless, the theoretical solution for the forward problem provided here, which was shown to be accurate for physiologically relevant transverse isotropic viscoelastic material properties, provides a rapid means of assessing the validity of other inversion algorithms by providing the ability to rapidly calculate the response of any transverse isotropic material with finite boundaries that create multiple reflections and standing wave patterns.

## ACKNOWLEDGMENTS

Thanks to D. Nicholls for identifying helpful references on Mathieu functions. Funding from NIH Grant No. AR071162 is acknowledged.

## APPENDIX

For elastic, plane waves traveling in a nearly incompressible, transversely isotropic (NITI) material, the assumed plane wave solution, $\boldsymbol{u}[\boldsymbol{x}, t] = u_0 \boldsymbol{m} e^{j(\omega t - k\boldsymbol{n}\cdot\boldsymbol{x})}$, satisfies the equation of motion

$$\nabla \cdot \boldsymbol{\sigma} = \rho \frac{\partial^2 \boldsymbol{u}}{\partial t^2}, \tag{A1}$$

where $\boldsymbol{\sigma}$ is a second order Cauchy stress tensor, $\nabla \cdot \boldsymbol{\sigma}$ is its divergence, $\rho$ is the material density, $\boldsymbol{u}$ is the displacement vector, and $t$ is time.[28] Also, the vectors $\boldsymbol{m}$ and $\boldsymbol{n}$ refer to the polarization direction of the displacement and the propagation direction, respectively. The elasticity tensor $\boldsymbol{K}$ of the NITI material model, in Voigt notation, relates stress $\boldsymbol{\sigma}$ to strain $\boldsymbol{\epsilon}$,

$$\boldsymbol{\sigma} = \begin{bmatrix} \sigma_{11} \\ \sigma_{22} \\ \sigma_{33} \\ \sigma_{23} \\ \sigma_{13} \\ \sigma_{12} \end{bmatrix} = \boldsymbol{K} \begin{bmatrix} \epsilon_{11} \\ \epsilon_{22} \\ \epsilon_{33} \\ 2\epsilon_{23} \\ 2\epsilon_{13} \\ 2\epsilon_{12} \end{bmatrix}, \tag{A2}$$

where $\boldsymbol{K}$ was given in Eq. (12). Substitution of the assumed solution into the equation of motion results in an eigenvalue problem, with three solutions $\lambda = \rho c^2$, which in the limit as $\kappa \to \infty$ are

$$\lambda_1 = \rho c_s^2 = \mu_\perp (1 + \phi \cos^2[\theta]), \tag{A3}$$

$$\lambda_2 = \rho c_f^2 = \mu_\perp(1 + \phi\cos^2[2\theta] + \zeta\sin^2[2\theta]), \tag{A4}$$

$$\lambda_3 = \rho c_p^2 \to \infty, \tag{A5}$$

where $c_s$ and $c_f$ are the slow and fast shear wave phase speeds, respectively, and $c_p$ is the longitudinal wave phase speed. The phase speeds approach these approximations closely for finite values of bulk modulus, $\kappa$, representative of soft biological tissue (within 1%–2% for $\kappa \approx 100\mu$).[29]


[1]H. E. von Gierke, H. L. Oestreicher, E. K. Franke, H. O. Parrack, and W. W. von Wittern, "Physics of vibrations in living tissues," J. Appl. Physiol. **4**, 886–900 (1952).
[2]X. Liang and S. Boppart, "Biomechanical properties of in vivo human skin from dynamic optical coherence elastography," IEEE Trans. Biomed. Eng. **57**, 953–959 (2010).
[3]K. Larin and D. Sampson, "Optical coherence elastography—OCT at work in tissue biomechanics," Biomed. Opt. Exp. **8**, 1172–1202 (2017).
[4]A. A. Khan, S. P. Kearney, and T. J. Royston, "Finite element based optimization of human fingertip optical elastography," ASME J. Eng. Sci. Med. Diag. Therapy **1**, 031007 (2018).
[5]Y. Yamakoshi, J. Sato, and T. Sato, "Ultrasonic imaging of internal vibration of soft tissue under forced vibration," IEEE Trans. Ultrason. Ferroelectr. Freq. Control **37**, 45–53 (1990).
[6]K. J. Parker, S. R. Huang, R. A. Musulin, and R. M. Lerner, "Tissue response to mechanical vibrations for 'sonoelasticity imaging,'" Ultrasound Med. Biol. **16**, 241–246 (1990).
[7]V. Dutt, R. R. Kinnick, R. Muthupillai, T. E. Oliphant, R. L. Ehman, and J. F. Greenleaf, "Acoustic shear-wave imaging using echo ultrasound compared to magnetic resonance elastography," Ultrasound Med. Biol. **26**, 397–403 (2000).
[8]T. Deffieux, J. L. Gennisson, J. Bercoff, and M. Tanter, "On the effects of reflected waves in transient shear wave elastography," IEEE Trans. Ultrason. Ferroelectr. Freq. Control **58**, 2032–2035 (2011).
[9]M. Wang, B. Byram, M. Palmeri, N. Rouze, and K. Nightingale, "Imaging transverse isotropic properties of muscle by monitoring acoustic radiation force induced shear waves using a 2-D matrix ultrasound array," IEEE Trans. Med. Imaging **32**, 1671–1684 (2013).
[10]R. Muthupillai, D. J. Lomas, P. J. Rossman, J. F. Greenleaf, A. Manduca, and R. L. Ehman, "Magnetic resonance elastography by direct visualization of propagating acoustic strain waves," Science **269**, 1854–1857 (1995).
[11]D. Klatt, T. K. Yasar, T. J. Royston, and R. L. Magin, "Sample interval modulation for the simultaneous acquisition of displacement vector data in magnetic resonance elastography: Theory and application," Phys. Med. Biol. **58**, 8663–8675 (2013).
[12]J.-L. Gennisson, S. Catheline, S. Chaffaiü, and M. Fink, "Transient elastography in anisotropic medium: Application to the measurement of slow and fast shear wave speeds in muscles," J. Acoust. Soc. Am. **114**, 536–541 (2003).
[13]D. Royer, J. L. Gennisson, T. Deffieux, and M. Tanter, "On the elasticity of transverse isotropic soft tissues (L)," J. Acoust. Soc. Am. **129**, 2757–2760 (2011).
[14]S. Chatelin, M. Bernal, T. Deffieux, C. Papadacci, P. Flaud, A. Nahas, C. Boccara, J.-L. Gennisson, M. Tanter, and M. Pernot, "Anisotropic polyvinyl alcohol hydrogel phantom for shear wave elastography in fibrous biological soft tissue: A multimodality characterization," Phys. Med. Biol. **59**, 6923–6940 (2014).
[15]S. Chatelin, J.-L. Gennisson, M. Bernal, M. Tanter, and M. Pernot, "Modelling the impulse diffraction field of shear waves in transverse isotropic viscoelastic medium," Phys. Med. Biol. **60**, 3639–3654 (2015).
[16]S. Aristizabal, C. Amador, B. Qiang, R. R. Kinnick, I. Z. Nenadic, J. F. Greenleaf, and M. W. Urban, "Shear wave vibrometry evaluation in transverse isotropic tissue mimicking phantoms and skeletal muscle," Phys. Med. Biol. **59**, 7735–7752 (2014).
[17]D. A. Shcherbakova, N. Debusschere, A. Caenen, F. Iannaccone, M. Pernot, A. Swillens, and P. Segers, "A finite element model to study the effect of tissue anisotropy on *ex vivo* arterial shear wave elastography measurements," Phys. Med. Biol. **62** 5245–5275 (2017).
[18]K. Chino, Y. Kawakami, and H. Takahashi, "Tissue elasticity of in vivo skeletal muscles measured in the transverse and longitudinal planes using shear wave elastography," Clin. Physiol. Funct. Imaging **37**, 394–399 (2017).
[19]N. C. Rouze, M. H. Wang, M. L. Palmeri, and K. R. Nightingale, "Finite element modeling of impulsive excitation and shear wave propagation in an incompressible, transversely isotropic medium," J. Biomech. **46**, 2761–2768 (2013).
[20]S. Papazoglou, J. Rump, J. Braun, and I. Sack, "Shear wave group velocity inversion in MR elastography of human skeletal muscle," Mag. Reson. Med. **56**, 489–497 (2006).
[21]M. A. Green, L. E. Bilston, and R. Sinkus, "*In vivo* brain viscoelastic properties measured by magnetic resonance elastography," NMR Biomed. **21**, 755–764 (2008).
[22]I. Sack, B. Beierbach, U. Hamhaber, D. Klatt, and J. Braun, "Non-invasive measurement of brain viscoelasticity using magnetic resonance elastography," NMR Biomed. **21**, 265–271 (2008).
[23]D. Klatt, S. Papazoglou, J. Braun, and I. Sack, "Viscoelasticity-based MR elastography of skeletal muscle," Phys. Med. Biol. **55**, 6445–6459 (2010).
[24]A. J. Romano, P. B. Abraham, P. J. Rossman, J. A. Bucaro, and R. L. Ehman, "Determination and analysis of guided wave propagation using magnetic resonance elastography," Magn. Reson. Med. **54**, 893–900 (2005).
[25]A. Romano, M. Scheel, S. Hirsch, J. Braun, and I. Sack, "In vivo waveguide elastography of white matter tracts in the human brain," Magn. Reson. Med. **68**, 1410–1422 (2012).
[26]Y. Feng, R. J. Okamoto, R. Namani, G. M. Genin, and P. V. Bayly, "Measurements of mechanical anisotropy in brain tissue and implications for transversely isotropic material models of white matter," J. Mech. Behav. Biomed. Mater. **23**, 117–132 (2013).
[27]S. Chatelin, I. Charpentier, N. Corbin, L. Meylheuc, and J. Vappou, "An automatic differentiation-based gradient method for inversion of the shear wave equation in magnetic resonance elastography: Specific application in fibrous soft tissues," Phys. Med. Biol. **61**, 5000–5019 (2016).
[28]J. L. Schmidt, D. J. Tweten, A. N. Benegal, C. H. Walker, T. E. Portnoi, R. J. Okamoto, J. R. Garbow, and P. V. Bayly, "Magnetic resonance elastography of slow and fast shear waves illuminates differences in shear and tensile moduli in anisotropic tissue," J. Biomech. **49**, 1042–1049 (2016).
[29]D. J. Tweten, R. J. Okamoto, J. L. Schmidt, J. R. Garbow, and P. V. Bayly, "Estimation of material parameters from slow and fast shear waves in an incompressible, transversely isotropic material," J. Biomech. **48**, 4002–4009 (2015).
[30]D. J. Tweten, R. J. Okamoto, and P. V. Bayly, "Requirements for accurate estimation of anisotropic material parameters by magnetic resonance elastography: A computational study," Magn. Reson. Med. **78**, 2360–2372 (2017).
[31]J. Guo, S. Hirsch, M. Scheel, J. Braun, and I. Sack, "Three-parameter shear wave inversion in MR elastography of incompressible transverse isotropic media: Application to in vivo lower leg muscles," Magn. Reson. Med. **75**, 1537–1545 (2016).
[32]P. V. Bayly and J. R. Garbow, "Pre-clinical MR elastography: Principles, techniques, and applications," J. Magn. Reson. **291**, 73–83 (2018).
[33]A. Kolipaka, S. R. Aggarwal, K. P. McGee, N. Anavekar, A. Manduca, R. L. Ehman, and P. A. Araoz, "Magnetic resonance elastography as a method to estimate myocardial contractility," J. Magn. Reson. Imaging **36**, 120–127 (2012).
[34]Y. Liu, T. J. Royston, D. Klatt, and E. D. Lewandowski, "Cardiac magnetic resonance elastography of the mouse: Initial results," Magn. Reson. Med. **76**, 1879–1886 (2016).
[35]A. Kolipaka, V. S. P. Illapani, P. Kalra, J. Garcia, X. Mo, M. Markl, and R. D. White, "Quantification and comparison of 4D-flow MRI-derived wall shear stress and MRE-derived wall stiffness of the abdominal aorta," J. Magn. Reson. Imaging **45**, 771–778 (2017).
[36]C. L. Johnson, M. D. McGarry, E. E. Houten, J. B. Weaver, K. D. Paulsen, B. P. Sutton, and J. G. Georgiadis, "Magnetic resonance elastography of the brain using multishot spiral readouts with self-navigated motion correction," Magn. Reson. Med. **70**, 404–412 (2013).
[37]L. Tan, M. D. J. McGarry, E. E. W. Van Houten, M. Ji, L. Solamen, J. Weaver, and K. D. Paulsen, "Gradient-based optimization for poroelastic and viscoelastic MR elastography," IEEE Trans. Med. Imaging **36**, 236–250 (2017).
[38]A. Caenen, M. Pernot, M. Peirlinck, L. Mertens, A. Swillens, and P. Segers, "An *in silico* framework to analyze the anisotropic shear wave mechanics in cardiac shear wave elastography," Phys. Med. Biol. **63**, 075005 (2018).

[39]B. Qiang, J. C. Brigham, S. Aristizabal, J. F. Greenleaf, X. Zhang, and M. W. Urban, "Modeling transversely isotropic, viscoelastic, incompressible tissue-like materials with application in ultrasound shear wave elastography," Phys. Med. Biol. **60**, 1289–1306 (2015).
[40]B. Qiang, J. C. Brigham, R. J. McGough, J. F. Greenleaf, and M. W. Urban, "Mapped Chebyshev pseudo-spectral method for simulating the shear wave propagation in the plane of symmetry of a transversely isotropic viscoelastic medium," Med. Biol. Eng. Comput. **55**, 389–401 (2017).
[41]H. L. Oestreicher, "Field and impedance of an oscillating sphere in a viscoelastic medium with an application to biophysics," J. Acoust. Soc. Am. **23**, 707–714 (1951).
[42]T. J. Royston, H. A. Mansy, and R. H. Sandler, "Excitation and propagation of surface waves on a viscoelastic half-space with application to medical diagnosis," J. Acoust. Soc. Am. **106**, 3678–3686 (1999).
[43]T. K. Yasar, T. J. Royston, and R. L. Magin, "Wideband MR elastography for viscoelasticity model identification," Magn. Reson. Med. **70**, 479–489 (2013).
[44]B. L. Schwartz, Z. Yin, T. K. Yasar, Y. Liu, A. A. Khan, A. W. Ye, T. J. Royston, and R. L. Magin, "Scattering and diffraction of elastodynamic waves in a concentric cylindrical phantom for MR elastography," IEEE Trans. Biomed. Eng. **63**, 2308–2316 (2016).
[45]B. L. Schwartz, Y. Liu, T. J. Royston, and R. L. Magin, "Axisymmetric diffraction of a cylindrical transverse wave by a viscoelastic spherical inclusion," J. Sound Vib. **364**, 222–233 (2016).
[46]J. Braun, H. Tzschatzsch, C. Korting, A. A. de Schellenberger, M. Jenderka, T. Driessle, M. Ledwig, and I. Sack, "A compact 0.5 T MR elastography device and its application for studying viscoelasticity changes in biological tissues during progressive formalin fixation," Magn. Reson. Med. **79**, 470–478 (2018).
[47]S. F. Othman, H. Xu, T. J. Royston, and R. L. Magin, "Microscopic magnetic resonance elastography ($\mu$MRE)," Magn. Reson. Med. **54**, 605–615 (2005).
[48]T. K. Yasar, D. Klatt, R. L. Magin, and T. J. Royston, "Selective spectral displacement projection for multifrequency MRE," Phys. Med. Biol. **58**, 5771–5781 (2013).
[49]Y. Liu, T. K. Yasar, and T. J. Royston, "Ultra wideband (500 Hz to 16 kHz) MR elastography for robust shear viscoelasticity model identification," Phys. Med. Biol. **59**, 7717–7734 (2014).
[50]S. Brinker, S. P. Kearney, T. J. Royston, and D. Klatt, "Simultaneous magnetic resonance and optical elastography acquisitions: Comparison of displacement images and shear modulus estimations using a single vibration source," J. Mech. Behav. Biomed. Mater. **84**, 135–144 (2018).
[51]S. M. Hasheminejad and A. Ghaheri, "Free vibration analysis of a finite-length isotropic solid elliptic cylinder using exact three dimensional elasticity theory," Appl. Math. Model. **37**, 8725–8741 (2013).
[52]J. C. Gutiérrez-Vega, R. M. Rodríguez-Dagnino, M. A. Meneses-Nava, and S. Chávez-Cerda, "Mathieu functions, a visual approach," Am. J. Phys. **71**, 233–242 (2003).
[53]K. Graff, *Wave Motion in Elastic Solids* (Dover, New York, 1991).
[54]G. Wolf, "Mathieu functions and Hill's equation," in *Digital Library of Mathematic Functions, Version 1.0.18* (National Institute of Standards and Technology, Gaithersburg, MD, 2018), Chap. 28.
[55]E. Cojocaru, "Mathieu functions computational toolbox implemented in MATLAB," *Mathieu Functions Toolbox v. 1.0*, arXiv:0811.1970v2 (2008).
[56]F. C. Meral, T. J. Royston, and R. L. Magin, "Rayleigh-Lamb wave propagation on a fractional order viscoelastic plate," J. Acous. Soc. Am. **129**, 1036–1045 (2011).
[57]See supplementary material at https://doi.org/10.1121/1.5064372 for animations of the theoretical model and FEA displacements, respectively, through a complete phase cycle.
[58]R. Namani, M. D. Wood, S. E. Sakiyama-Elbert, and P. V. Bayly, "Anisotropic mechanical properties of magnetically aligned fibrin gels measured by magnetic resonance elastography," J. Biomech. **42**, 2047–2053 (2009).
[59]E. C. Qin, R. Sinkus, G. Geng, S. Cheng, M. Green, C. D. Rae, and L. E. Bilston, "Combining MR elastography and diffusion tensor imaging for the assessment of anisotropic mechanical properties: A phantom study," J. Magn. Reson. Imaging **37**, 217–226 (2013).
[60]E. H. Clayton, R. J. Okamoto, and P. V. Bayly, "Mechanical properties of viscoelastic media by local frequency estimation of divergence-free wave fields," J. Biomech. Eng. **135**, 021025 (2013).
[61]M. A. Green, G. Geng, E. Qin, R. Sinkus, S. C. Gandevia, and L. E. Bilston, "Measuring anisotropic muscle stiffness properties using elastography," NMR Biomed. **26**, 1387–1394 (2013).
[62]T. J. Royston, T. Spohnholtz, and W. A. Ellingson, "Use of nondegeneracy in nominally axisymmetric structures for fault detection with application to cylindrical geometries," J. Sound Vib. **230**, 791–808 (2000).